

Use of synchrotron X-rays for direct observation of wear damage in optically-opaque contacts by means of CT imaging and X-ray diffraction

J. Alekseyev^{a,*}, M. Williamson^b, J.E. Huber^a, O.V. Magdysyuk^c, S. Michalik^c, T.J. Marrow^b

^a Department of Engineering Science, University of Oxford, Oxford OX1 3PJ, United Kingdom

^b Department of Materials, University of Oxford, Oxford OX1 3PH, United Kingdom

^c Diamond Light Source Ltd., Harwell Science and Innovation Campus, Didcot OX11 0DE, United Kingdom

ARTICLE INFO

Keywords:

X-ray tomography
X-ray diffraction
Wear
Wear debris

ABSTRACT

In a simulated in-situ experiment annular contacts of 6082-T6 aluminium alloy were first exposed to various degrees of fretting wear, before synchrotron X-ray CT and diffraction were applied to examine the extent and development of wear damage. The wear volumes measured and development of the wear rate were consistent with the mathematical wear model of Fillard, Iordanoff & Berthier. Thickness and porosity of the worn zone were measured and the contact area between wearing elements estimated. Developments of residual strain and tribologically transformed structure were investigated through X-ray diffraction. This study demonstrates, for the first time, the value and viability of observing and quantifying wear through combination of X-ray CT and diffraction opening a path towards in-situ observations of wear.

1. Introduction

In studies of wear, observing the changes caused by friction of surfaces is of paramount interest. These changes include roughening and folding of surfaces [1], creation, accumulation and transport of wear debris [2,3], chemical reactions of the wear debris and wearing bodies with the atmosphere and/or lubricants [4–7], as well as subsurface changes, such as recrystallisation and grain refinement [8–12]. Understanding the nature and role of these processes is crucial for enhancing the understanding of wear, and for the development of accurate wear models [13]. Beside measuring the extent of wear in terms of volume or mass of material removed, other quantities are also of interest to a tribologist, including surface roughness, real area of contact, size of wear debris particles, thickness of the tribologically transformed structure, and grain size in the wear affected zone.

While many techniques have been developed for quantifying phenomena associated with wear, most of them require the wearing contact to be dismantled in order to be subjected to weighing, profilometry, microscopy, metallography, electron back-scatter diffraction etc. Traditional techniques enabling the observation of wear with the sample elements in contact and under load include the use of transparent counter-bodies and position sensors for measurement of the thinning of the sample elements [14,15]. However, these techniques are limited and

often require special material combinations that do not necessarily replicate in-service conditions.

For the study of metal-to-metal contacts, a technique enabling the surface and sub-surface effects of wear to be studied without the wear process being disrupted would be of great value. In this way, the wear could be observed and quantified directly, thus also enabling models predicting processes such as initiation of wear, growth of the debris bed and the generation of tribologically transformed structure to be tested. X-ray methods have been successfully used to quantify wear-related phenomena: Zanini et al. [16] and Hejjaji et al. [17] measured post-wear surface profiles using ex-situ X-ray computed tomography showing that appropriately fine resolution can be obtained; discussion of X-ray diffraction for studying crystal structure changes in wear are provided by Lee [18], with examples of in-situ diffraction on wear affected structures being published by Reid et al. [19] demonstrating the ability to observe wear-related stresses. Several studies [20–23] have shown the viability of 2D X-ray radiography for observing wear between a variety of optically opaque materials. Zhang et al. [24,25] applied X-ray computed tomography to observe the real area of contact between artificially textured surfaces. The ability to establish the real area of contact through X-ray imaging is of particular interest. While mathematical models linking surface profiles and real area of contact exist [26], see also discussions in [27,28] as well as the finite element

* Corresponding author.

E-mail address: jure.alekseyev@chch.ox.ac.uk (J. Alekseyev).

<https://doi.org/10.1016/j.triboint.2022.107809>

Received 31 May 2022; Received in revised form 13 July 2022; Accepted 23 July 2022

Available online 26 July 2022

0301-679X/© 2022 The Authors. Published by Elsevier Ltd. This is an open access article under the CC BY license (<http://creativecommons.org/licenses/by/4.0/>).

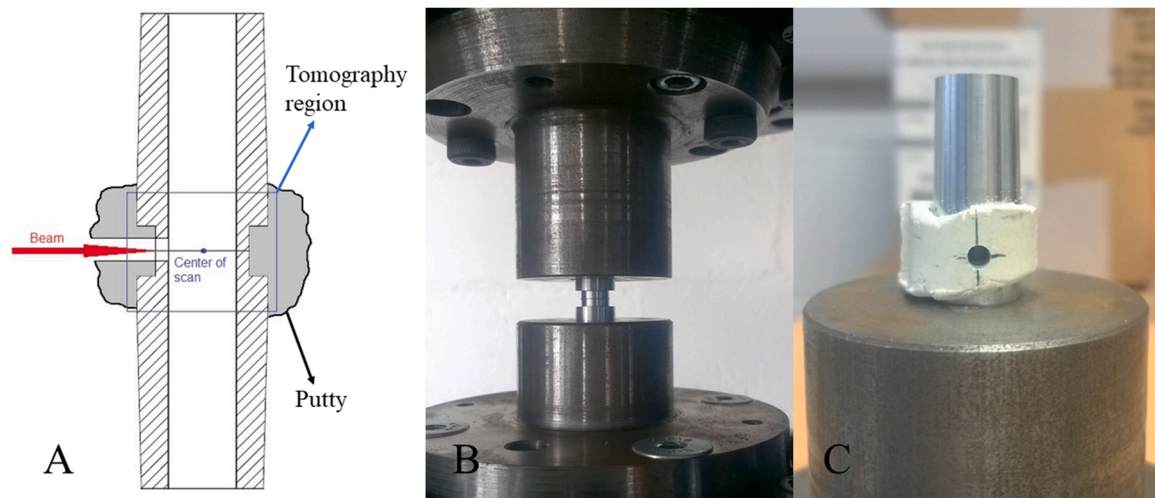


Fig. 1. The wear sample. Sample elements and binding putty in cross-section A) Wear rig. Wear sample after wear under axial load B), After putty setting and hole drilling C).

modelling of Zhang et al. [24,25], they require knowledge of both the surface profiles and material properties. Establishing post-wear surface profiles traditionally requires separation and cleaning of the wear bodies, removing the influence of wear debris accumulation on the final result. Alekseyev et al. [29] demonstrated that X-ray computed tomography can be used to observe and quantify the wear process (including the real area of contact) in a worn metal-metal contact, with the wear sample elements remaining in contact and under load.

This work presents the results of a proof-of-concept study aimed at demonstrating the combined application of synchrotron X-ray computed tomography and diffraction to undisturbed worn contacts. Wear samples were bonded in epoxy putty whilst under load to preserve the worn-in condition. The experiment thus straddles the boundary between in-situ and ex-situ approaches, since the wear and X-ray examinations are separate, but the contact remains undisturbed and wear debris can be observed in-situ. A series of samples with different numbers of wear cycles was examined, each sample representing a separate point in the progressive development of the wear process. The benefits of using a synchrotron facility are their much greater brightness, which allows for a greater size of the wear sample, as well as the ability to accommodate larger and heavier experimental equipment [30–33], which is conducive to more complex experimental set-ups. In this work, the JEEP beamline I12 at the Diamond Light Source was used, with capabilities for both tomography and diffraction experiments [30,34].

2. Experiment

Two sets of samples were prepared, each set representing a wear experiment running at a constant normal force, with each sample representing one point in the development of wear from the unworn to steady-state wear condition. A total of 15 wear samples were prepared (each consisting of two sample elements). 7 were worn at a normal force of 510 N (nominal contact pressure of 25 MPa) for 50, 100, 200, 500, 1000, 2500 and 5000 cycles respectively. 7 additional samples were worn at normal force of 300 N (nominal contact pressure of 15 MPa) for 50, 100, 200, 500, 1000, 2500 and 5000 cycles. One further sample was bonded under a normal force of 510 N without any wear, to produce a control sample to represent the initial (unworn) condition. The samples were worn using a Z100 compression-torsion loading frame (Zwick-Roell, Germany). In all cases, wear was generated by applying a reciprocating rotary motion, using a frequency of 0.5 Hz and an imposed angular amplitude of 3° , see Fig. 1B. Examinations of the fretting loops (please see the supplementary materials) established that the effective angular displacement reduced with the progress of the experiment from

nearly 100% of the imposed displacement at start to $\geq 2.5^\circ$ in steady state which corresponds to effective linear amplitude of $\approx 142 \mu\text{m}$ at the median radius. Temperature in the experimental room was between 17 and 20°C , relative air humidity between 38%–49%.

As in the work of Alekseyev et al. [29] an annular contact was used, with an external diameter of 7.5 mm and internal diameter of 5.5 mm. Sample elements were made of aluminium alloy 6082 in the T6 temper on account of its low X-ray attenuation. Initially, all samples had a finely turned finish on the annular contact surfaces. Samples were connected to the sample holders using Morse taper #1 to ensure good positioning accuracy and reliable transfer of torque from sample holder to the samples.

At the end of each wear test, the sample had its elements bonded using UniBond Express Repair epoxy putty (contained within a temporary PVC sleeve mould and left under full normal load to cure for 24 h). A special procedure was developed to remove the bonded sample without causing undue stresses at the worn interface, which is described in detail in supplementary materials. A radial hole (2.5 mm diameter) was drilled through the putty and the wear zone (Fig. 1C) to provide a path for the transmitted diffraction beam to examine just one side of the sample (Fig. 1A). Using energy dispersive X-ray spectroscopy, the putty was determined to contain an even distribution of spots measuring some μm in size with high concentrations of Ca, Mg and Si, which is consistent with mineral filler particles.

2.1. X-ray diffraction and tomography measurements

Samples were set up with their longitudinal axis perpendicular to the beam with the radial drilled hole and the beam coaxial. For diffraction, a monochromatic beam with an energy of 58.7 keV was used, combined with a CdTe Pilatus area detector and a LaB₆ powder-calibrated sample-detector distance of 691 mm. A horizontal ‘letter-box’ beam of $0.25 \times 0.05 \text{ mm}$ was obtained using slits. A 1.5 mm line scan was made by translating the sample vertically in steps of 0.02 mm to generate 76 diffraction points across the worn region. The exposure time was 10 s per diffraction point. The software package DAWN [35–37] was employed to azimuthally integrate the calibrated 2D patterns.

For the X-ray computed tomography of each sample, a field of view of $8 \times 5.5 \text{ mm}$ was observed by a PCO.edge camera (module 3 optics), with 1800 projections taken over a 180° rotation; using an exposure time of 0.05 s per projection. A lower beam energy of 53 keV was used for improved attenuation contrast. This indicates ample reserve of capacity for studying wear in more attenuating materials, such as ferrous alloys. The voxel size of the reconstructed tomographs was $3.24 \mu\text{m}$,

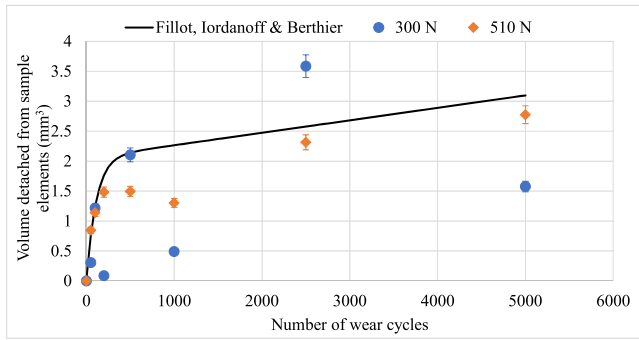


Fig. 2. Volume detached from the sample elements as measured, with fit to the model of Fillot, Iordanoff and Berthier.

with tomographs being stored in 16-bit quality. The FBP algorithm [38] as a part of Astra Toolbox [39] implemented in the in-house developed program Savu [40] was used for reconstruction of tomography data; additionally with the Paganin filter plugin [41], automatic determination of the centre of rotation plugin [42] and ring artefact removal plugin [43].

3. Results and discussion

During the wear process, the separation of the sample holders gradually changes on account of changes in the sample shape. The volume of material displaced by the wear process was obtained directly from the axial position output of the Zwick-Roell machine by scaling it with the nominal contact area, Fig. 2. While this method is crude compared to mass loss measurements, the latter were not possible due to the need to preserve the contact and debris bed undisturbed. Fig. 2 also shows a fit to the numerical model of Fillot, Iordanoff and Berthier [44–47], which is briefly reviewed here.

The Fillot, Iordanoff and Berthier model is described by three basic equations [45]: Eq. 1 describes the particle detachment flow rate (Q_d , the rate at which material is removed from the wearing bodies), Eq. 2 describes the particle ejection flow rate (Q_e , the rate at which the wear debris is ejected from the contact). M_b denotes the mass of wear debris entrapped between wearing surfaces, the change of M_b with wear is given by Eq. 3. Particle detachment constant C_d , particle ejection constant C_e and the maximum entrapped mass M_{max} (if sufficient quantity of debris is entrapped, particle detachment no longer occurs) are parameters determining the particle detachment in, and ejection from, the contact and thus the process of wear.

$$Q_d(t) = \frac{C_d(M_{max} - M_b(t))}{\rho S} \quad (1)$$

$$Q_e(t) = \frac{C_e M_b(t)}{\rho S} \quad (2)$$

$$\frac{dM_b}{dt} = Q_d(t) - Q_e(t) = \frac{C_d(M_{max} - M_b(t))}{\rho S} - \frac{C_e M_b(t)}{\rho S} \quad (3)$$

Solving Eq. 3 (assuming $M_b(0) = 0$ as a boundary condition) and dividing by debris density ρ and nominal contact area S enables the debris bed thickness H to be calculated, as well as integrating Eq. 1 to determine the total amount of material removed (Eq. 5). Calculated mass losses were re-calculated into volumes to compare with the measurements.

$$H(t) = \frac{C_d M_{max}}{(C_d - C_e) \rho S} \left(1 - e^{-\frac{C_d - C_e}{\rho S} t} \right) \quad (4)$$

$$V_{wear} = \frac{C_d C_e M_{max} t}{(C_d - C_e) \rho S} + \frac{C_d M_{max}}{C_d - C_e} \left(1 - e^{-\frac{C_d - C_e}{\rho S} t} \right) \quad (5)$$

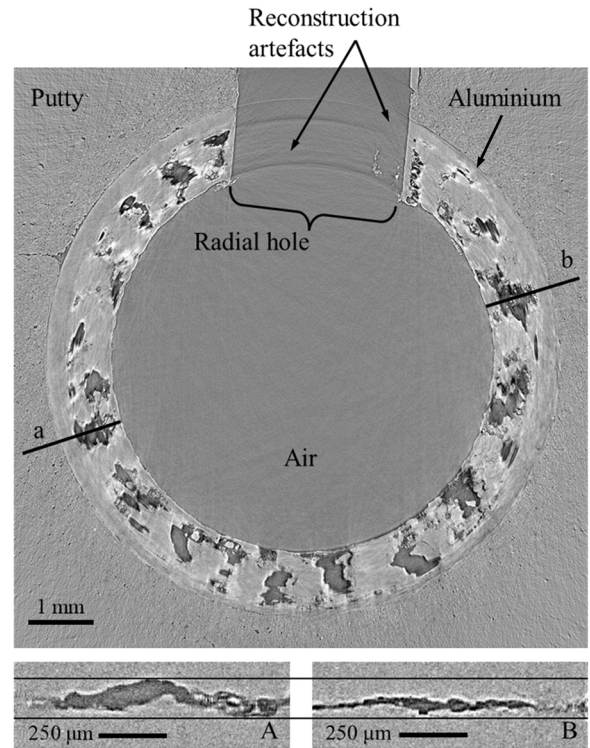


Fig. 3. Axial tomography section, showing characteristic components. Lines a and b are lines of radial section, the respective magnified radial sections (marked A and B) being shown below. The horizontal lines in radial sections mark the limits of the wear scar in these two sections. Sample was worn for 1000 cycles at normal force of 510 N.

The quantity of wear is not significantly dependent on the normal force, which is consistent with experimental evidence of Hintikka et al. [48,49] showing that wear in full annular contacts becomes independent of normal force, if the force is sufficiently large. Since the difference between data points collected at 300 N and 510 N is within the experimental scatter, the model of Fillot, Iordanoff and Berthier was manually fitted to the pooled datasets. Here it should be borne in mind, that in a true in-situ experiment (rather than a simulated one, as presented here) each data point would be the result of the wear process continuing from the previous data point. In practice this means that in a true in-situ experiment it would be impossible for there to be less volume loss after 1000 cycles than after 500 (as it occurred when using normal force of 510 N) or that there would be more wear after 2500 cycles than after 5000 (as it occurred here when using 300 N). The scatter encountered here, while unfortunate, further illustrates the sensitivity of the wear process to a variety of factors and therefore the value of being able to directly observe the progress of wear within one wear sample. The parameter values used to generate the fit were: $C_d = 105 \text{ mgs}^{-1} \text{m}^{-1}$, $C_e = 1.3 \text{ mgs}^{-1} \text{m}^{-1}$ and $M_{max} = 5.44 \text{ mg}$. The fit indicates that the steady state condition is attained after approximately 500 cycles. The trajectory generated is also consistent with the experimental results published by [9,50–52], which is consistent with the Fillot, Iordanoff & Berthier model being a general model of wear.

3.1. Tomography - Observations of Worn Surface

A typical example of a horizontal tomography section through the wear scar is shown in Fig. 3, showing the putty, aluminium sample, the radial hole drilled through the side of the sample and the wear damage. Contrast in the image represent differences in X-ray attenuation coefficient. At the edges, some space propagation artefacts are also visible as an unintended consequence of a relatively long sample to detector

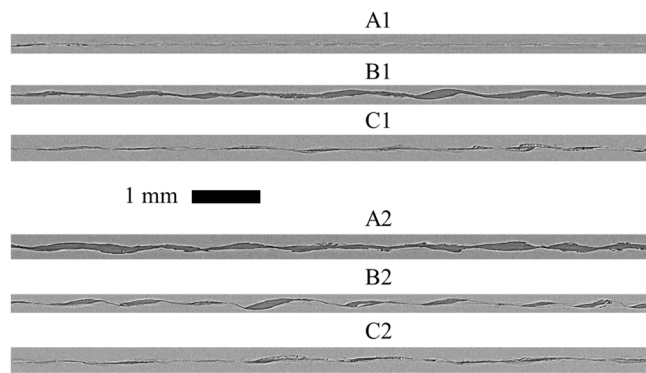


Fig. 4. 'Unwrapped' tomography data, showing cross-section of the worn zone along the median circumference of the sample. Wear at 300 N, after 200 cycles A1) after 500 cycles B1) after 2500 cycles C1) Wear at 510 N, after 200 cycles A2) after 500 cycles B2) after 2500 cycles C2).

distance. Fig. 3A-B shows example radial sections through the worn zone at locations marked, which shows the porous region between the surfaces of the first bodies. Using MATLAB code developed at the Oxford's Department of Material Science, the annular sample can be 'unwrapped', which enables sections along circumference to be visualised as planar sections. Fig. 4 presents sections made along the median circumference, showing the undulating surface created by 200, 500 and

2500 wear cycles of six wear samples (three at 300 N and 510 N of normal force respectively).

Fig. 5 shows a series of horizontal axial sections obtained at intervals over a distance of $\sim 65 \mu\text{m}$ across the wear zone in two samples, each subjected to 50 wear cycles at 300 N and 510 N. Sections A1 and A2 lie just at the top of the wear zone, sections E1 and E2 just at the bottom, as defined in Fig. 3. The roughening and folding of the surface, which is characteristic of wear damage, initiates around the inner edge of the annulus and is limited to material close to this edge. Initiation of wear at the inner edge is consistent with modelling work of [53], which demonstrates that in this annular sample geometry, there is a radial contact pressure gradient with the pressure being highest at the inner edge. Fig. 6 shows samples after 100 wear cycles; the wear damage can be seen spreading outwards in the radial direction (compare Fig. 6-C2 with Fig. 5-C2). After 500 wear cycles (Fig. 7, here the sections span a distance of $\sim 130 \mu\text{m}$), which corresponds to the onset of a steady state wear regime (as indicated by the trend in Fig. 2), the wear damage extends almost across the entire annular surface (Fig. 7-C1 and -C2).

The progress of wear with the number of cycles at both levels of normal load is illustrated in Figs. 8 and 9. The sections selected are equidistant from the edges of the wear zone in each sample, as defined in Fig. 3. These sections illustrate in a qualitative manner the radial spread of wear damage, with the steady state condition attained after approximately 500 cycles when the wear damage extends across the annular contact.

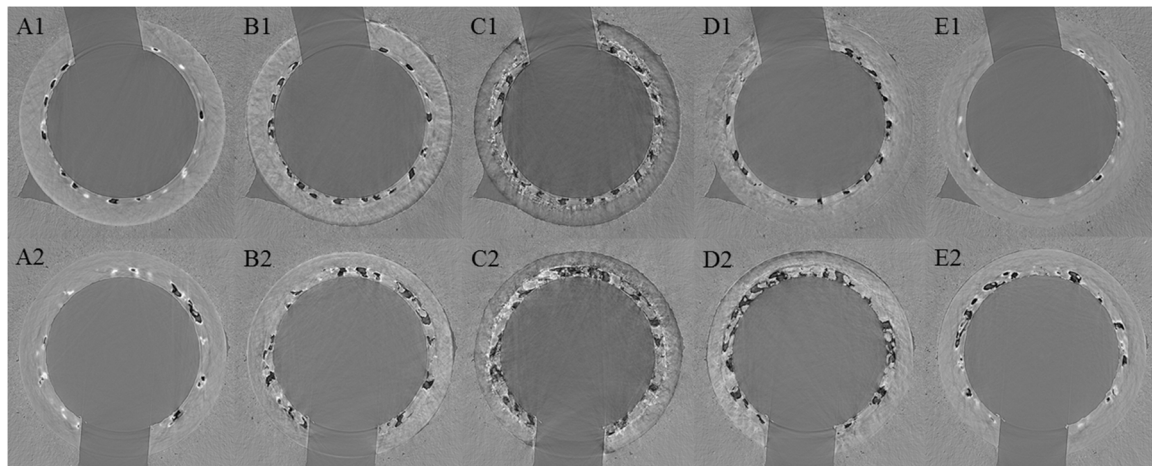


Fig. 5. Axial sections of the worn region after 50 wear cycles; distance between each section is $16.2 \mu\text{m}$. A1-E1 show wear at 300 N, A2-E2 wear at 510 N.

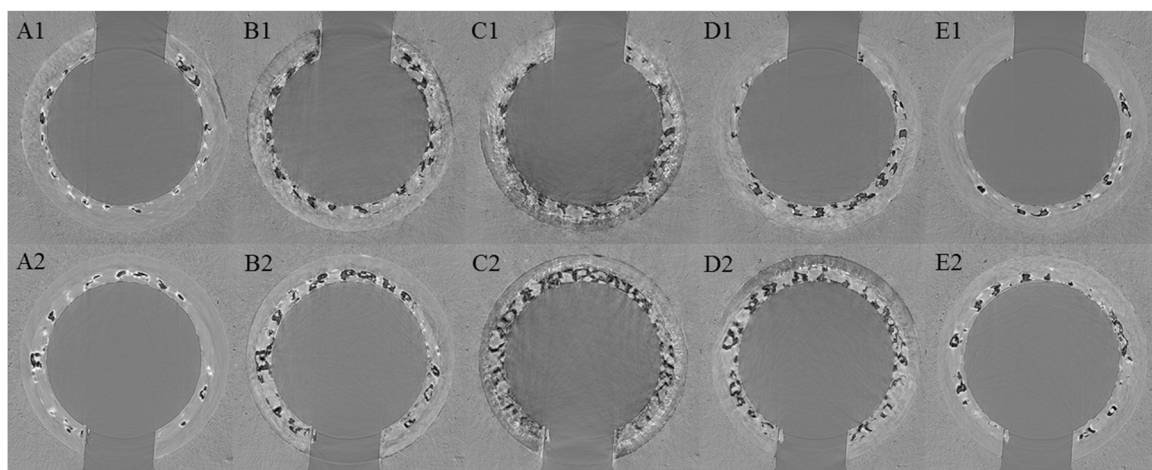


Fig. 6. Axial sections of the worn region after 100 cycles; distance between each section is $16.2 \mu\text{m}$. A1-E1 show wear at 300 N, A2-E2 wear at 510 N.

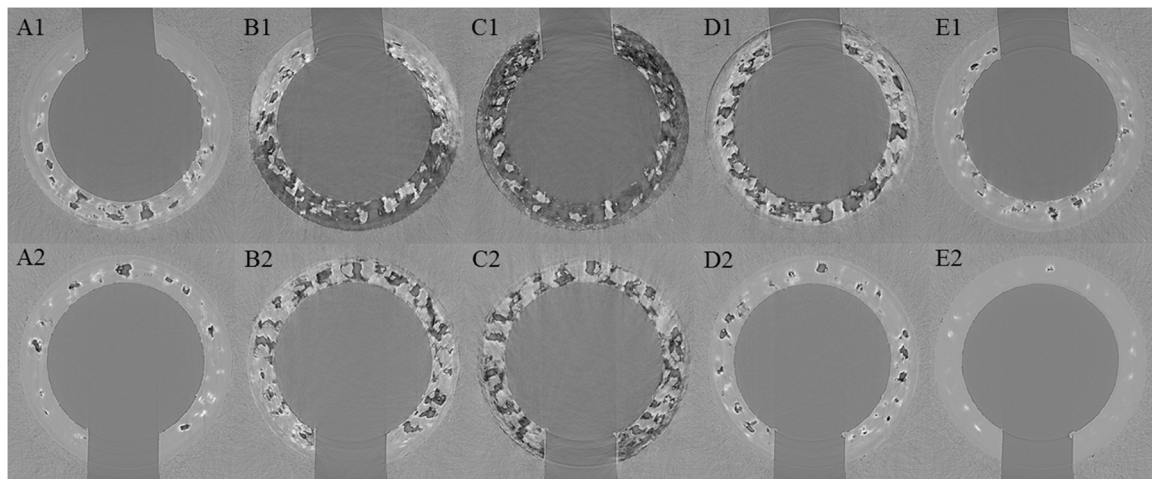


Fig. 7. Axial sections of the worn region after 500 cycles; distance between each section is 32.4 μm . A1-E1 show wear at 300 N, A2-E2 wear at 510 N.

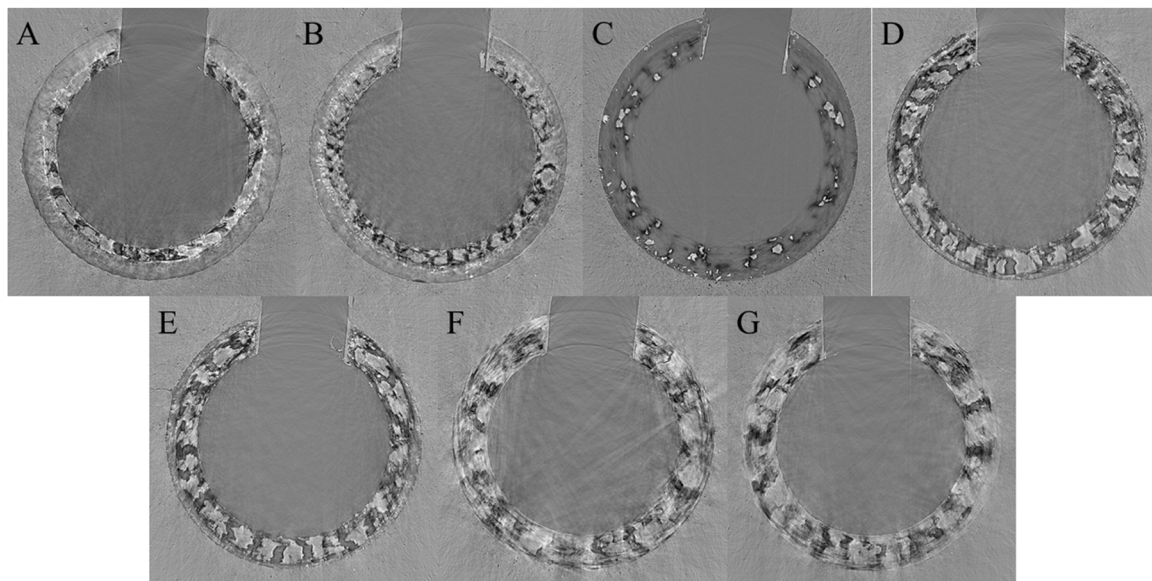


Fig. 8. Axial cross-sections through the middle of the worn zone (normal force 510 N); 50 cycles A) 100 cycles B) 200 cycles C) 500 cycles D) 1000 cycles E) 2500 cycles F) 5000 cycles G).

Despite being worn to different degrees, the wear zones shown in Figs. 8 and 9 all show patterning of the wear zone into patches of material, giving the appearance of leopard spots. This is the result of undulation of the worn surface, as shown in Fig. 4. The patches are roughly periodic, appearing at regular intervals around the circumference. The angular separation between the centres of raised patches in the wear zone was measured on each wear sample using the sections shown in Figs. 8 and 9. The frequency distribution of the observed separation angles is shown in Fig. 10, indicating an approximate periodicity with period $10^\circ - 30^\circ$ that is not affected by the normal load. The average angular separation is $17.7^\circ \pm 0.2^\circ$ (standard deviation 5.0°) for samples worn at 300 N and $18.0^\circ \pm 0.2^\circ$ (standard deviation 6.6°) for samples worn at 510 N. This period is approximately 6 times the angular displacement amplitude. While a roughly even distribution of material around the circumference is expected (to avoid pile-up of material leading to uneven contact pressure) there is no immediately apparent reason for the observed periodicity.

3.2. Total thickness of the wear scar

The total thickness of the wear scar can be estimated by identification of the sections in which the wear scar begins and ends (with an absolute error of ± 4 sections or $\pm 12.96 \mu\text{m}$), as shown in Fig. 3. The total wear scar thickness is an upper bound on the thickness of the debris bed layer. In addition, Fig. 11A also shows the debris bed thickness predicted using the Fillot, Iordanoff and Berthier model [45,46], (Eq. 4) and the parameter values used to generate the fit in Fig. 2. The predicted debris bed thickness was found to roughly match the development of total wear scar depth in both magnitude and shape (a rapid initial increase followed by a steady plateau). However, the empirical measurements of total wear scar thickness show a 'hump' peaking at about 200 cycles, rather than a monotonic increase predicted by the model. This trajectory is very similar to typical trajectories of friction coefficient during the wear experiment and could indicate that the relation between the total wear scar depth and the debris bed thickness is not perfectly linear. Total thickness of the wear scar was compared to the wear volume (Fig. 11B), which shows that once the wear commenced, the wear scar thickness develops rapidly, and then increases gradually with wear

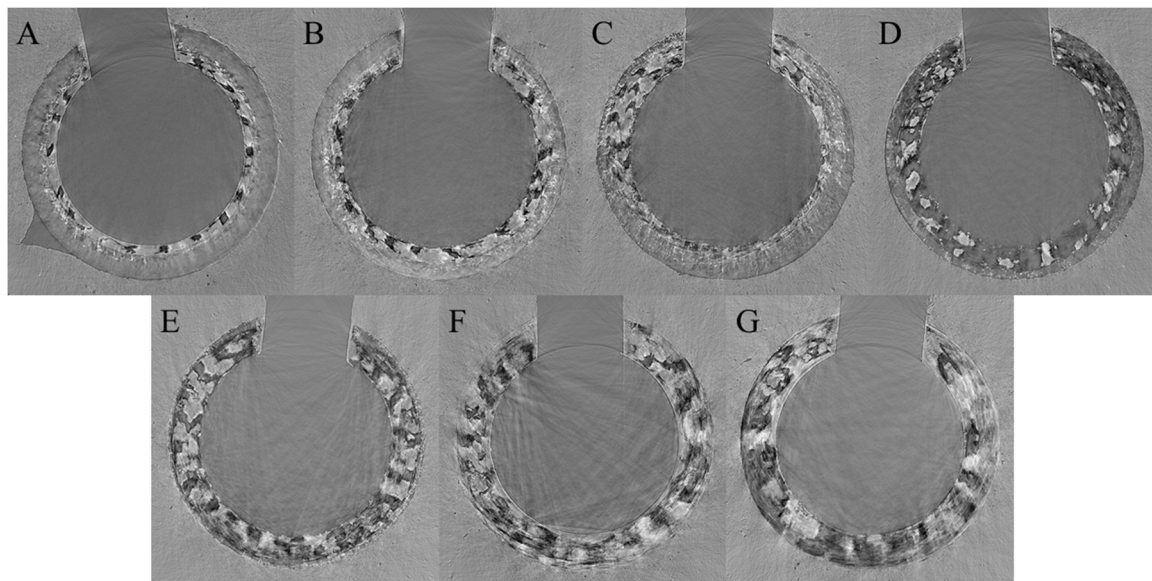


Fig. 9. Axial cross-sections through the middle of the worn zone (normal force 300 N); 50 cycles A) 100 cycles B) 200 cycles C) 500 cycles D) 1000 cycles E) 2500 cycles F) 5000 cycles G).

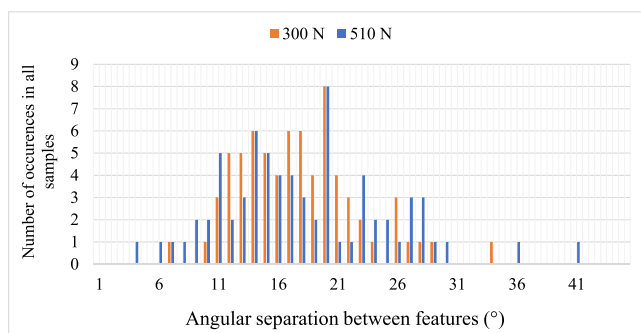


Fig. 10. Frequency distribution of raised patch angles measured at both levels of normal force (histogram bins of 1°).

volume before stabilizing at a steady state value that is independent of the wear volume once the wear volume reaches $\sim 1.5\text{--}2\text{ mm}^3$. This is coincident with the onset of steady state that is shown in Figs. 2 and 11A.

3.3. Contact porosity

In the present study, contact porosity is defined as the percentage of the wear zone volume which is not metal nor metal oxide. Here, the wear zone volume is defined as the nominal contact area multiplied with the total wear scar thickness. The contact porosity can thus be estimated by examining radial sections through the worn zone. The procedure is described in detail in the [supplementary materials](#). In short, 16 radial sections were taken from each tomograph and submitted to threshold-based segmentation (using ImageJ) to determine the area not corresponding to metal or metal oxide. From this, the equivalent height of the empty area was determined; the mean average equivalent height multiplied with the nominal contact area gives the volume of the void within the wear zone. The porosity values for each of the samples are shown in Fig. 12. The error bars show the standard error of mean for each data point. Contact porosity increases sharply in the initial stage of wear, before settling at a steady-state value of $\approx 10\%$.

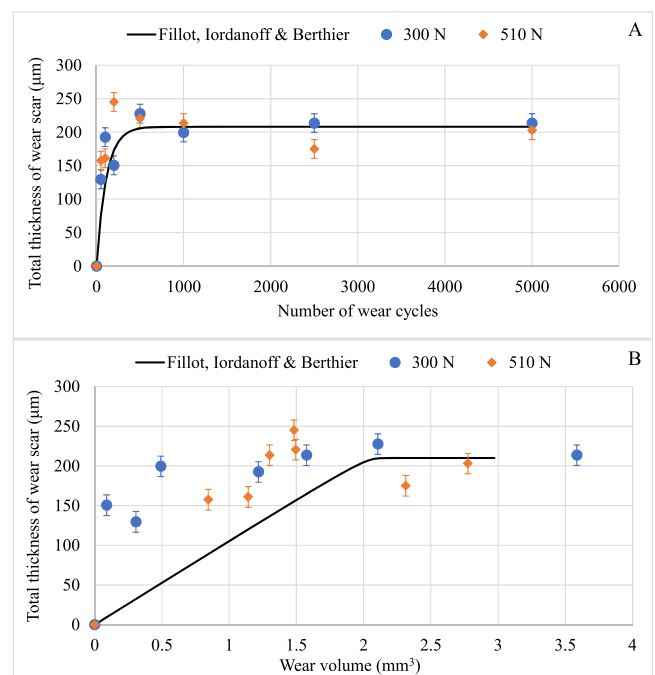


Fig. 11. Total thickness of wear scar and the debris bed thickness predicted by the model of Fillot, Iordanoff & Berthier. Shown as a function of the number of wear cycles A) Shown as a function of wear volume B).

3.4. Real area of contact

Using the method described in [29], the real area of contact between the worn surfaces can be estimated. The process starts with generating a 3D render of the air region of the tomograph in Avizo software. The exact shape of the render depends on the threshold point set in Avizo. An image of the render along the axis of rotation is made. The gaps in the air region, represent continuity of metal between the sample elements and thus local contact of the sample elements. Using ImageJ, the area of these gaps is then measured to establish the size of the contact area between worn bodies. Selected examples of real areas of contact are

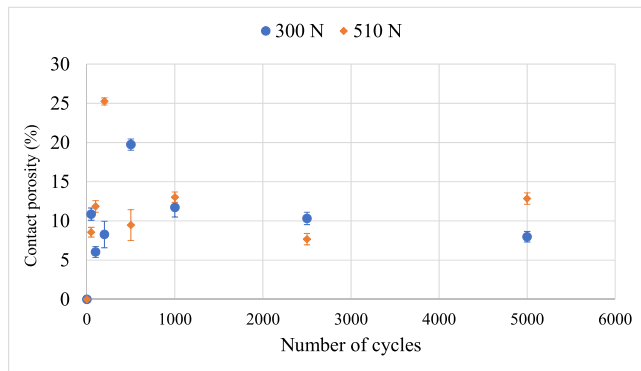


Fig. 12. Contact porosity versus cycle number at each load level.

shown in Fig. 13.

As seen in Fig. 13D, an artefact occurred at the edges of the radial hole; to remove it, a thin region at either edge of the hole was excluded from the calculation of the contact area (see Fig. 14).

The real area of contact is greatest before wear and reduces rapidly to near zero ($\approx 0.5\%$ of nominal contact area) before increasing again to a low steady-state value ($\approx 5\%$). Estimating the real area relied on manually thresholding the tomography data in Avizo software, introducing a degree of human decision in the end result. Error bars were estimated by moving the thresholding value 1000 points above and below the chosen value (which conservatively represents the range of realistic threshold values), to find the largest resulting deviation in calculated area.

3.5. Diffraction analysis of the wear zone

The purpose of the X-ray diffraction measurements was to investigate wear-induced changes to the structure of the sample material. Numerous researchers have demonstrated that wear typically causes restructuring of the material immediately underneath the wear scar [7,11,12,54–56] characterised by extensive plastic straining, work hardening and grain refinement.

As described in Section 3.3, the worn contact is porous, causing the intensity of the diffraction peaks to drop when the porous worn region

moves through the beam. Fig. 15 shows example data for the intensity of the most intense Bragg reflection {220} (details about the spectra collected and peak identification methods can be found in [supplementary materials](#)). The diffraction data were integrated over an angle of

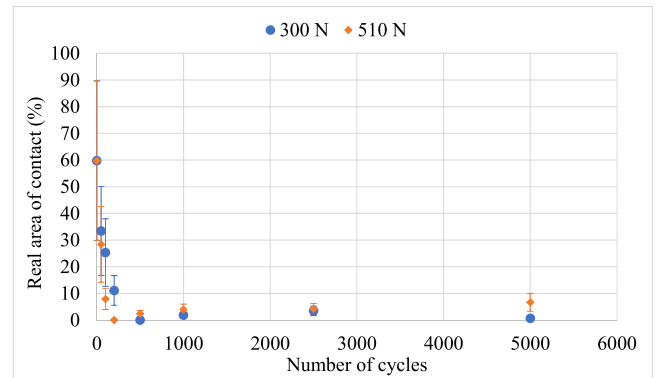


Fig. 14. Real contact area expressed in % of nominal contact area.

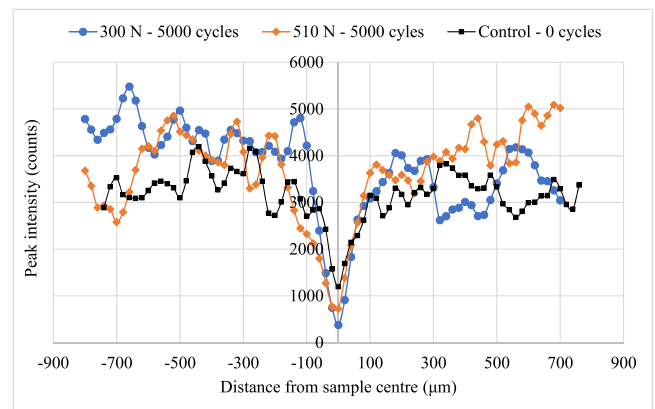


Fig. 15. Peak intensities for the 220 crystal planes as a function of position within sample after 5000 cycles compared to the unworn control sample.

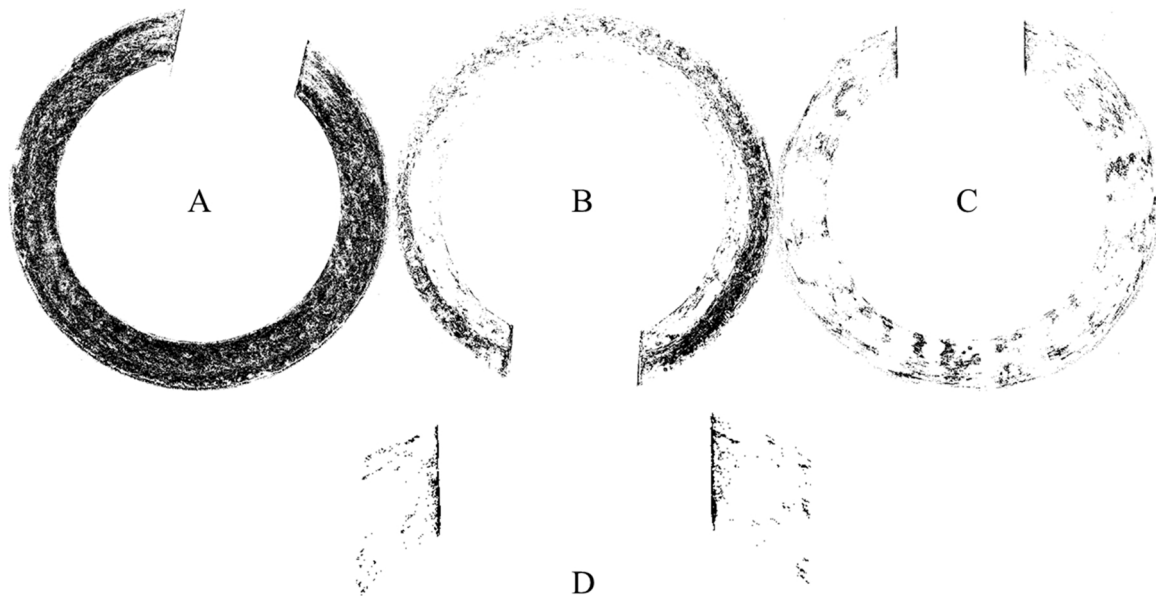


Fig. 13. Real areas of contact, black showing the metal-to-metal contact. Unworn contact A), Normal force 510 N, 100 wear cycles B), Normal force 510 N, 5000 wear cycles C), Detail of the area around radial hole D).

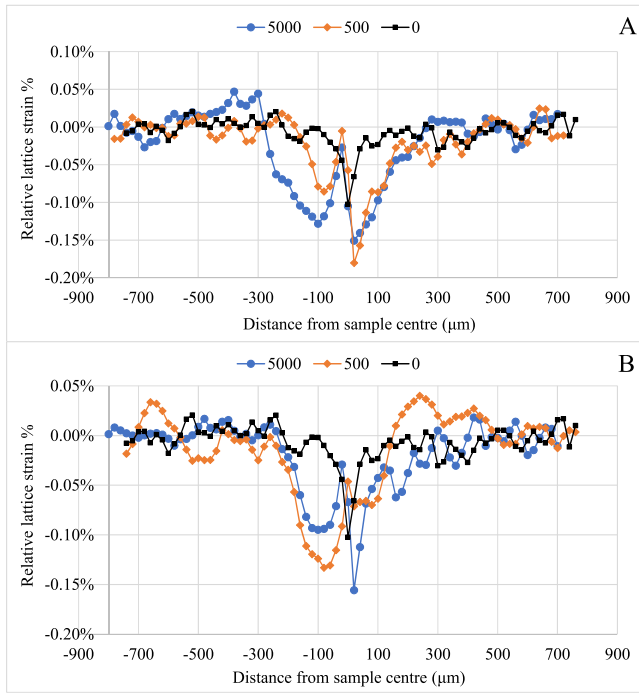


Fig. 16. Residual lattice strain as a function of position at different numbers of cycles. Normal force: 510 N A) 300 N B).

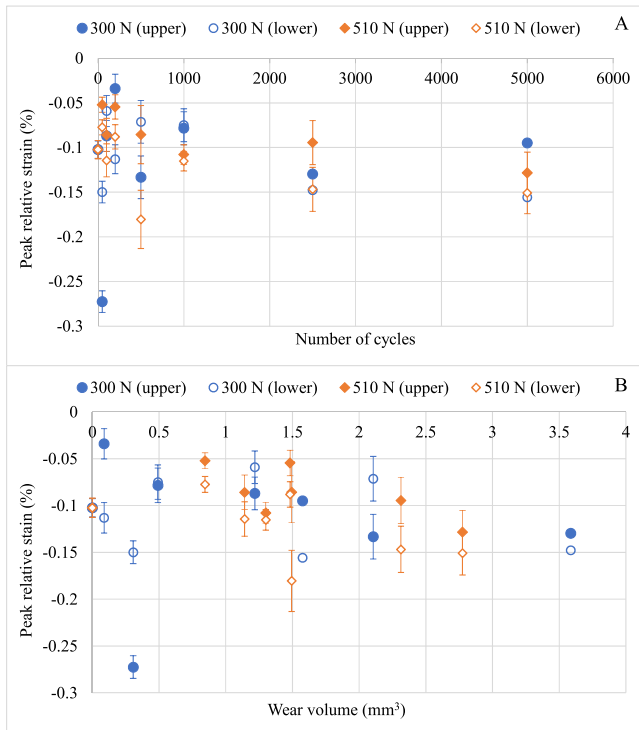


Fig. 17. Greatest magnitude of relative strain observed in each sample as a function of cycle number A) and wear volume measured B).

7.5° of either side of azimuthal angle of 0°. Azimuthal angle of 0° corresponds with the plane of contact within the wear samples. All strain results calculated thus reflect hoop strain within the annuli of the samples. The results presented here focus on the 220 family of planes, as it consistently showed a strong signal intensity, with a clear dip at the contact. This peak was also least affected by experimental measurement

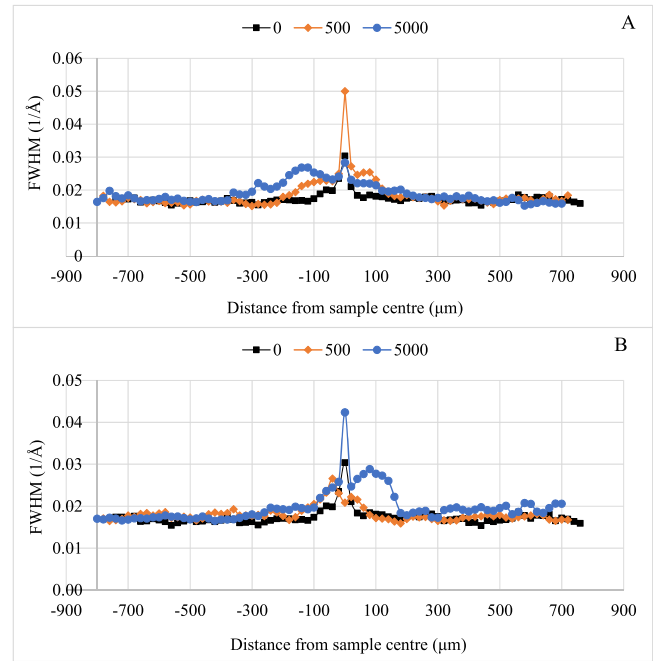


Fig. 18. FWHM for the 220 reflection, at 510 N of normal force A) at 300 N of normal force B).

noise. It was assumed, that the point with the lowest peak intensity represents the centre of the respective sample and all distances are shown with respect to this centre.

The residual elastic lattice strain was determined using the fractional shift of the {220} diffraction peak, relative to the stress-free state that was assumed to exist in material that was far away from the wear region. As each sample element is a separate piece of material, 15 far-away points were averaged from each end of the sample, with the elastic strain in each sample element calculated relative to its respective far away average; as before, the point with lowest peak intensity was considered the centre of the sample and thus the dividing point between both sample elements. Representative examples of the spatial distribution of the relative elastic strain are presented in Fig. 16A and B.

The distribution of residual strain generally shows a 'double dip' in the contact region (see for example the 5000 cycle line in Fig. 16A). The position of the central 'spike' which divides the dip in two, corresponds with the location of minimum signal intensity, indicating that this is the artefact caused by signal loss due to contact porosity. The largest magnitudes of elastic strain for each sample element are shown in Fig. 17 as a function of the number of cycles (Fig. 17A) and wear volume (Fig. 17B). As each sample consists of two sample elements, the two largest magnitudes can be extracted from each sample (one for each element) which are denoted 'upper' or 'lower' depending on which sample element they occur in. The error bars show the standard error of mean for the strain intensity.

In a similar manner, the changes in peak width can be examined. In the region around the wear zone, the 220 peak broadens noticeably, indicating a rearrangement of the crystal lattice and changes in crystal grain size. Examples of distribution of peak width (expressed as full width at half maximum; FWHM) are shown in Fig. 18.

The development of the residual strains and peak widths suggests different wear processes occurring at different stages. In the initial stage, the surface is roughened by surface folding and/or material transfer, possibly in a manner suggested by [11] causing large asperities to form. This is consistent with the appearance of the wear zone as shown in Fig. 8C-D and Fig. 9C. The large asperities are eventually worn away as the debris bed builds and a mechanically-worked/recrystallised layer is formed. This layer also retains elastic strain beneath the surface,

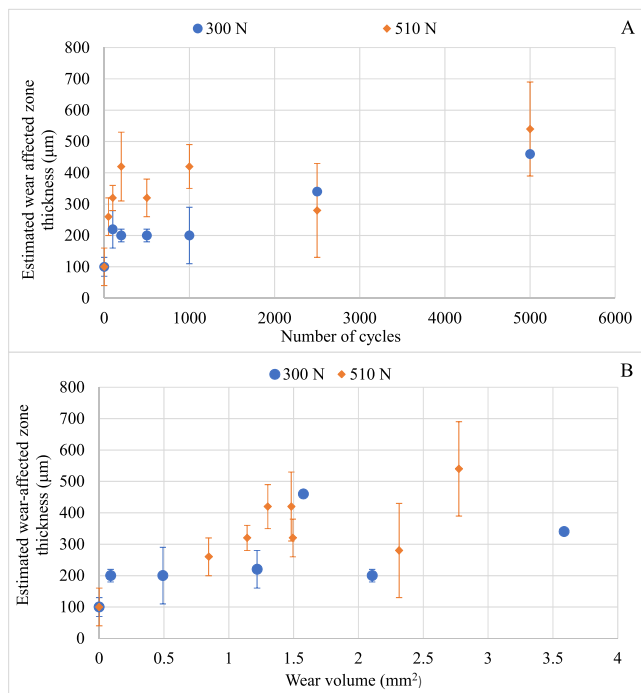


Fig. 19. Estimated thickness of the wear affected zone as a function of number of cycles A) and as a function of wear volume B).

possibly due to indentation of the virgin material by debris particles.

Thickness of the wear affected zone can be estimated from the peak broadening data. Here, the wear affected zone is defined as the combination of the wear scar itself, plus the strained/recrystallized layer. Secondly, the limits of the wear affected zone are defined as points where the peak broadening first exceeds the far-away average for the respective sample element by more than two standard deviations. Fig. 19A shows thickness of the wear affected zone as a function of cycle number and Fig. 19B a function of wear volume.

4. Conclusions

Using X-ray synchrotron tomography and diffraction, we have demonstrated measurement of several wear-related phenomena without disturbing the contact. The measurements included quantity of material removed, wear scar thickness, contact porosity, real area of contact, residual strain distribution, and estimates of the thickness of the wear affected zone. The measurements of contact porosity and real area of contact could be particularly valuable in studying permeability of a contact to fluids, heat or electrical currents. The amount of material removed and the wear scar thickness were in good qualitative agreement with a model by Fillot, Iordanoff and Berthier, increasing rapidly in the initial stage of wear before transitioning to the respective steady-state conditions. Real area of contact decreases rapidly with the onset of wear, before stabilizing at a low value. As the wear progresses, compressive hoop strain accumulates underneath the worn surface, its peak absolute value first increasing and then saturating with the number of cycles. The evolution of several parameters indicates that the transition between the transient and steady-state wear regime occurs between 200 and 500 wear cycles with the parameter either peaking or beginning to saturate in this region.

Using traditional approaches such information could not be obtained without destroying the contact and possibly the sample elements themselves. Lack of disruption to the wear zone is vitally important for any attempt to observe the progress of wear in one wear sample, which hitherto was only possible with optically transparent samples. It is also doubtful, if traditional techniques could supply the entire range of the

information obtained, since some of the phenomena studied can only be observed with the wearing surfaces remaining in contact.

While in this study only a small number of data points was gathered and the wear and X-ray parts of the experiments were conducted separately, the approach demonstrates the potential for detailed in-situ observation of wearing metallic contacts. The combination of the non-destructive nature of the approach and the capability of synchrotron beamlines to provide short imaging times and accommodate complex sample environments, make it realistic to wear the sample on the beamline and observe it many times during the course of wear. The large quantity of data thus produced can be used for monitoring the development and progress of wear and assessing the validity of models predicting the same. A full in-situ experiment with a single sample per load level is planned for future investigation.

Declaration of Competing Interest

The authors declare that they have no known competing financial interests or personal relationships that could have appeared to influence the work reported in this paper.

Data Availability

Data will be made available on request.

Acknowledgments

This work was supported by Rolls Royce plc through contract number 4800000925 and Cornerstone Prosperity Partnership. It was carried out with the support of Diamond Light Source, instrument I12, experiment MG27537-1. Avizo facilities were funded through the EPSRC Grant EP/M02833X/1 "University of Oxford: experimental equipment upgrade".

The authors wish to thank Dr Kalin Dragnevski of the Oxford University of Engineering Science for his help with the energy dispersive X-ray spectroscopy and access to the appropriate equipment; Dr Igor Dyson for lending equipment used in production of the samples and the staff of the Staff-Student workshop for their help with manufacture of the sample holders.

Tribology International Statement of originality.

As corresponding author, I Jure Aleksejev, hereby confirm on behalf of all authors that:

The manuscript submitted presents original research carried out by the authors at the University of Oxford and Diamond Light Source. 2) The manuscript has not been published previously and is not under consideration for publication elsewhere. 3) The manuscript does not contain material which has been published previously, by the current authors or by others, of which the source is not explicitly cited in the paper.

Appendix A. Supporting information

Supplementary data associated with this article can be found in the online version at [doi:10.1016/j.triboint.2022.107809](https://doi.org/10.1016/j.triboint.2022.107809).

References

- [1] Mahato A, Guo Y, Sundaram NK, Chandrasekar S. Surface folding in metals: a mechanism for delamination wear in sliding. *Proc R Soc A* 2014;vol. 470.
- [2] Godet M, Play D, Berthe D. An attempt to provide a unified treatment of tribology through load carrying capacity, transport, and continuum mechanics. *J Lubr Technol* 1980;vol. 102:153–64.
- [3] Godet M. The third-body approach: a mechanical view of wear. *Wear* 1984;vol. 100:437–52.
- [4] Kalin M. Influence of flash temperatures on the tribological behaviour in low-speed sliding: a review. *Mater Sci Eng A* 2004;vol. 374:390–7.
- [5] Kalin M, Vizintin J. Comparison of different theoretical models for flash temperature calculation under fretting conditions. *Tribol Int* 2001;vol. 34:831–9.

- [6] Fouvry S, Arnaud P, Mignot A, Neubauer P. Contact size, frequency and cyclic normal force effects on Ti6Al4V fretting wear processes: an approach combining friction power and contact oxygenation. *Tribology Int* 2017;vol. 113:460–73.
- [7] Kirk A, Shipway P, Sun W, Bennett C. The effect of frequency on both the debris and the development of the tribologically transformed structure during fretting wear of a high strength steel. *Wear* 2019;Vols. 426–427:694–703.
- [8] Swalla D, Neu R, McDowell D. Microstructural characterization of Ti-6Al-4V subjected to fretting. *J Tribology* 2004;vol. 126:809–16.
- [9] Bidville A, Favero M, Stadelmann P, Mischler S. Effect of surface chemistry on the mechanical response of metals in sliding tribocorrosion systems. *Wear* 2007;vol. 263:207–17.
- [10] Stoyanov P, Pinsler D, Schlarb T, Scherge M, Schwaiger R. Dependence of tribofilm characteristics on the running-in behavior of aluminum–silicon alloys. *J Mater Sci* 2015;vol. 50:5524–32.
- [11] Nurmi V, Hintikka J, Juoksukangas J, Honkanen M, Vippola M, Lehtovaara A, et al. The formation and characterization of fretting-induced degradation layers using quenched and tempered steel. *Tribol Int* 2019;vol. 131:258–67.
- [12] Juoksukangas J, Nurmi V, Hintikka J, Honkanen M, Vippola M, Lehtovaara A, et al. Cracks and degradation layers in large flat-on-flat fretting contact with steels and cast iron. *Tribology Int* 2020;vol. 145.
- [13] Meng HC, Ludema KC. Wear models and predictive equations: their form and content. *Wear* 1995;Vols. 181–183:443–57.
- [14] Zivic F, Babic M, Mitrovic S, Vencel A. Continuous control as alternative route for wear monitoring by measuring penetration depth. *J Alloy Compd* 2011;vol. 509: 5748–54.
- [15] Alekseev J, Clark Z, Huber J, Hills D. Experimental investigation of debris entrapment in annular contacts. *J Eng Tribology* 2020;vol. 235:687–97.
- [16] Zanini F, Carmignato S, Savio E, Affatato S. Uncertainty determination for X-ray computed tomography wear assessment of polyethylene hip joint prostheses. *Precis Eng* 2018;vol. 52:477–83.
- [17] Hejjaji A, Zitouni R, Crouzeix L, Le Roux S, Collombet F. Surface and machining induced damage characterization of abrasive water jet milled carbon/epoxy composites specimens and their impact on tensile behaviour. *Wear* 2017;Vols. 376–377:1356–64.
- [18] Lee H. Analysis of sliding wear mode on annealed steel by X-ray diffraction technique. *Wear* 2004;vol. 256:657–63.
- [19] Reid A, Simpson C, Martinez I, Kabra S, Connolley T, Magdysyuk O, et al. Measurement of strain evolution in overloaded roller bearings using energy dispersive X-ray diffraction. *Tribol Int* 2019;vol. 140.
- [20] Chandrasekaran M, Batchelor A. In situ observation of sliding wear tests of butyl rubber in the presence of lubricants in an X-ray microfocus instrument. *Wear* 1997; vol. 211:35–43.
- [21] Fu Y, Batchelor A, Loh L. Study on fretting wear behavior of laser treated coatings by X-ray imaging. *Wear* 1998;vol. 218:250–60.
- [22] Fu Y, Batchelor A, Loh N. Revealing the hidden world of fretting wear processes of surface coatings by X-ray imaging. *Surf Coat Technol* 1998;vol. 107:133–41.
- [23] Chandrasekaran M, Batchelor A, Loh N. Direct observation of frictional seizure of mild steel sliding on aluminum by X-ray imaging Part I: Methods. *J Mater Sci* 2000; vol. 35:1589–96.
- [24] Zhang F, Liu J, Ding X, Wang R. Experimental and finite element analyses of contact behaviors between non-transparent rough surfaces. *J Mech Phys Solids* 2019;vol. 126:87–100.
- [25] Zhang F, Liu J, Ding X, Yang Z. A discussion on the capability of X-ray computed tomography for contact mechanics investigations. *Tribol Int* 2020;vol. 145.
- [26] Greenwood J, Williamson J. Contact of nominally flat surfaces. *Proc R Soc A* 1966; vol. 295(300–319).
- [27] O'Callaghan P, Probert S. Prediction and measurement of true area of contact between solids. *Wear* 1987;vol. 120:29–49.
- [28] Paggi M, Ciavarella M. The coefficient of proportionality k between real contact area and load, with new asperity models with new asperity models. *Wear* 2010;vol. 268(1020–1029).
- [29] Alekseev J, Lim Y, Huber J, Hofmann F, Marrow J. In-situ X-ray tomography of wear – a feasibility study. *Tribol Int* 2020;vol. 150.
- [30] "Diamond Light Source, [Online]. Available: <https://www.diamond.ac.uk/Instruments/Imaging-and-Microscopy/I12/Experiments-in-EH1.html>. [Accessed 25 February 2020].
- [31] "European Synchrotron Radiation Facility, [Online]. Available: <https://www.esrf.fr/cms/live/live/en/sites/www/home/UsersAndScience/Experiments/StructMaterials/ID19.html>. [Accessed 07 August 2021].
- [32] "Advanced Photon Source, [Online]. Available: https://www.aps.anl.gov/Beamlines/Directory/Details?beamline_id=2.
- [33] "Diamond Light Source, [Online]. Available: <https://www.diamond.ac.uk/Instruments/Imaging-and-Microscopy/I13.html>. [Accessed 7 August 2021].
- [34] Drakopoulos M, Connolley T, Reinhard C, Atwood R, Magdysyuk O, Vo N, et al. I12: the joint Engineering, Environment and Processing (JEEP) beamline at Diamond Light Source. *J Synchrotron Radiat* 2015;vol. 22:828–38.
- [35] Basham M, Filik J, Wharmby M, Chang P, El Kassaby B, Gerrig M, et al. Data analysis workbench (DAWN). *J Synchrotron Radiat* 2015;vol. 22:853–8.
- [36] Filik J, Ashton A, Chang P, Chater P, Day S, Drakopoulos M, et al. Processing two-dimensional X-ray diffraction and small-angle scattering data in DAWN 2. *J Appl Cryst* 2017;vol. 50:959–66.
- [37] M. Hart, M. Drakopoulos and C. Reinhard, Complete elliptical ring geometry provides energy and instrument calibration for synchrotron-based two-dimensional X-ray diffraction, *Journal of Applied Crystallography*, vol. 46, p. 1249–1260.
- [38] G. Ramachandran and A. Lakshminarayanan, Three dimensional reconstruction from radiographs and electron micrographs: Application of convolution instead of Fourier transforms, *Proceedings of Natural Academy of Sciences*, vol. 68, pp. 2236–2240, 1971.
- [39] Gilbert P. Iterative methods for the reconstruction of three-dimensional objects from their projections. *J Theor Biol* 1972;vol. 36:105–17.
- [40] N. Wadson and M. Basham, Savu: a Python-based, MPI framework for simultaneous processing of multiple, N-dimensional, large tomography datasets, 2016.
- [41] Paganin D, Mayo S, Gureyev T, M. P.R, Wilkins S. Simultaneous phase and amplitude extraction from a single defocused image of a homogeneous object. *J Microsc* 2002;vol. 206:33–40.
- [42] Vo N, Drakopoulos M, Atwood R, Reinhard C. Reliable method for calculating the center of rotation in parallel beam tomography. *Opt Express* 2014;vol. 22: 19078–86.
- [43] Vo N, Atwood R, Drakopoulos M. Superior techniques for eliminating ring artifacts in X-ray micro-tomography. *Opt Express* 2018;vol. 26:28396–412.
- [44] Fillot N, Iordanoff I, Berthier Y. A granular dynamic model for the degradation of material. *J Tribol* 2004;vol. 126:606–14.
- [45] Fillot N, Iordanoff I, Berthier Y. Simulation of wear through mass balance in a dry contact. *J Tribol* 2005;vol. 127:230–7.
- [46] Fillot N, Iordanoff I, Berthier Y. Wear modelling and the third body concept. *Wear* 2007;vol. 262:949–57.
- [47] Fillot N, Iordanoff I, Berthier Y. Modelling third body flows with discrete element method - a tool for understanding wear with adhesive particles. *Tribol Int* 2007; vol. 40:973–81.
- [48] Hintikka J, Lehtovaara A, Mäntylä A. Fretting-induced friction and wear in large flat-on-flat contact with quenched and tempered steel. *Tribol Int* 2015;vol. 92: 191–202.
- [49] Hintikka J, Lehtovaara A, Mäntylä A. Third particle ejection effects on wear with quenched and tempered steel fretting contact. *Tribol Trans* 2016;vol. 60:70–8.
- [50] Blades L, Hills D, Nowell D, Evans K, Smith C. An exploration of debris types and their influence on wear rates in fretting. *Wear* 2020;Vols. 450–451.
- [51] Blades L, Hills D, Nowell D, Evans K, Smith C. The effects of external loading on low displacement wear rates of unlubricated steels. *Wear* 2022;Vols. 490–491.
- [52] Rynio C, Hattendorf H, Klöwer J, Eggeler G. On the physical nature of tribolayers and wear debris after sliding wear in a superalloy/steel tribosystem at 25 and 300 °C. *Wear* 2014;vol. 317:26–38.
- [53] Hintikka J, Mäntylä A, Vaara J, Frondelius T, Lehtovaara A. Stable and unstable friction in fretting contacts. *Tribol Int* 2019;vol. 131:73–82.
- [54] Zhou ZR, Sauger E, Liu JJ, Vincent L. Nucleation and early growth of tribologically transformed structure (TTS) induced by fretting. *Wear* 1997;vol. 212:50–8.
- [55] Sauger E, Fouvry S, Ponsonnet L, Kapsa P, Martin J, Vincent L. Tribologically transformed structure in fretting. *Wear* 2000;vol. 245:39–52.
- [56] Sauger E, Ponsonnet L, Martin J, Vincent L. Study of the tribologically transformed structure created during fretting tests. *Tribol Int* 2000;vol. 33:743–50.